Available online at www.sciencedirect.com
ScienceDirect
Magnetic Resonance Imaging 26 (2008) 337–346
MAGNETIC RESONANCE IMAGING

Simultaneous magnetic resonance imaging of diffusion anisotropy and diffusion gradient

Jie Huang[a,*], David C. Zhu[a,b,c]

[a]Department of Radiology, Michigan State University, East Lansing, MI 48824, USA
[b]Department of Psychology, Michigan State University, East Lansing, MI 48824, USA
[c]Cognitive Imaging Research Center, Michigan State University, East Lansing, MI 48824, USA

Received 18 April 2007; revised 18 July 2007; accepted 8 August 2007

Abstract

The theory of diffusion gradient-weighted MRI (DGWI) is presented in this paper. The Bloch–Torrey equation was modified to include the effect of intravoxel spatial-location variation of water diffusion (diffusion gradient) on MRI signal, in addition to the effect of intravoxel spatial-direction variation of water diffusion (diffusion anisotropy). An analytical solution for a diffusion-encoding spin-echo pulse sequence was derived. Unlike water diffusion which attenuates the image signal intensity, this newly derived solution relates the spatial gradient of the water diffusion with the phase of the image signal. This novel MRI technique directly measures both the water diffusion and its spatial gradient, and thus offers a noninvasive imaging tool to simultaneously investigate the intravoxel inhomogeneity and anisotropy of tissue structures. In addition, as demonstrated with our preliminary data, this new method may be utilized to delineate the interfaces of tissues with different diffusion. This method is an extension of the successful diffusion tensor MRI (DTI), but requires no additional data acquisition. In addition to the measured diffusion tensor, this new method provides measurements of the spatial derivatives of the three principal diffusivities of the tensor, thereby providing additional information for improving white matter fiber tractography.

Keywords: MRI; DTI; Diffusion gradient-weighted MRI

1. Introduction

Diffusion-weighted MRI (DWI) combines magnetic resonance imaging principles with molecular diffusion effects in MR signal to reveal diffusion characteristics of water molecules in tissues [1]. Molecular diffusion refers to the random Brownian motion of molecules resulting from thermal agitation. In the presence of a magnetic field gradient, molecular diffusion causes a phase dispersion of the transverse magnetization, resulting in a reduction to the MRI signal [2,3]. In comparison to free water diffusion, the diffusive motion of water molecules in a tissue is influenced by the tissue microstructure. The degree of restriction that is encountered by water diffusion in the tissue is reflected in the diffusion coefficient or diffusivity, i.e., the stronger the restriction, the smaller the diffusivity. Since its successful application in detecting brain ischemia [4,5], DWI has become a routine clinical imaging tool.

In DWI, the effect of water diffusion along one direction is selected by the direction of the probing magnetic field gradient pulses [6]. Water diffusion in solution is isotropic. In biological tissues, however, the presence of various tissue components that restrict the Brownian motion in certain directions may render the water diffusion anisotropic. Water diffusion-induced signal loss in a DWI image voxel results from the total contribution of all water molecules within the voxel. For many tissues such as gray matter (GM), when averaged over the macroscopic scale of the voxel, the overall effect of tissue components on the Brownian motion is almost the same in every direction. Macroscopically, the diffusion remains isotropic and is characterized by a constant diffusivity. However, in highly structured tissues such as white matter, molecular mobility in these tissues may not be the same in all directions, rendering the diffusion anisotropic. This spatial direction-related diffusion (diffusion anisotropy) is better characterized by a diffusion tensor in DTI [7–9].

* Corresponding author. Tel.: +1 517 355 0120x246; fax: +1 517 432 2849.
E-mail address: jie@rad.msu.edu (J. Huang).

0730-725X/$ – see front matter © 2008 Elsevier Inc. All rights reserved.
doi:10.1016/j.mri.2007.08.008

Inhomogeneous tissue structures yield diffusion variation from one location to another location. Intravoxel spatial location-related diffusion (diffusion gradient) has not been explored yet. When diffusion is slower (more restriction) in one location than another, it exhibits a spatial diffusion gradient between the two locations. For example, when diffusion is slower in the left half of a voxel than in the right half, it produces a spatial gradient from left to right within the voxel. This diffusion gradient is characterized by the spatial derivative of the diffusion coefficient. Since these diffusion gradients are caused by the inhomogeneous tissue structures, a measurement of the diffusion gradients with MRI will offer a noninvasive imaging tool for investigating intravoxel inhomogeneous tissue structures. In biological tissues, including highly structured ones, the intravoxel diffusion gradient in most places is not expected to be large, except at the boundary of two structures having markedly different diffusion properties. An animal study showed that, during the acute stage of brain ischemia, water diffusion is decreased in the ischemic territory by as much as 50% [10]. This 50% reduction in diffusion would yield a large diffusion gradient across the boundary between the ischemic territory and the intact tissue. The sharp contrast between the large gradient at the tissue interface and small gradients within the tissues provides a quantity to delineate the interface precisely.

One important application of DTI is white matter fiber tractography [11]. When DTI is applied to mapping anisotropic diffusion in white matter fiber bundles, assuming the direction of the eigenvector for the primary eigenvalue of the diffusion tensor aligns along the fiber direction, the connection of these eigenvectors forms the fiber track. When the bundles converge or diverge inside a voxel, diffusion on the converging side is more restricted than that on the diverging side, resulting in a spatial diffusion gradient along the fiber direction [12]. Thus, the measurement of diffusion gradient may provide useful information in improving white matter fiber tracking. In this work, we provide a novel MRI technique to measure both diffusion anisotropy and diffusion gradient simultaneously.

In this study we first present the solution of the modified Bloch–Torrey equation to include the effect of intravoxel diffusion gradient on MRI signal. As will be seen, we found that, unlike diffusion which attenuates the MRI signal intensity, the diffusion gradient causes a phase shift to the MRI signal. This result is not a surprise as a diffusion gradient could be viewed as a "pseudo-flow," and this "pseudo-flow" should induce a phase shift to the MRI signal just like a fluid flow would produce a similar phase shift when either bipolar gradients are applied or when a refocusing pulse is inserted between two unipolar gradients. Then we present a method for detection and correction of the diffusion-encoding gradient pulse-induced Eddy current (EC) artifacts in phase images. These EC artifacts are large, unavoidable and can render the phase measurement unreliable if not corrected. Finally, we present a preliminary experiment which qualitatively demonstrates a potential application of the presented technique in delineating the interface of two tissues with markedly different diffusion properties.

2. Theory

2.1. Solution of the modified Bloch–Torrey equation

In the absence of bulk fluid flow, the Bloch–Torrey equation can be modified to include the effect of anisotropic molecular diffusion [6]:

$$\frac{\partial \vec{M}}{\partial t} = \gamma \vec{M} \times \vec{H} - \frac{(M_x \hat{i} + M_y \hat{j})}{T_2} - \frac{(M_0 - M_z)\hat{k}}{T_1} + \vec{\nabla} \cdot \overleftrightarrow{D} \cdot \vec{\nabla} \vec{M} \tag{1}$$

where $\vec{M}$ is the magnetization, $\vec{H}$ the magnetic field, γ the gyromagnetic ratio of protons, T_1 the longitudinal relaxation time, T_2 the transverse relaxation time, $\vec{\nabla} \equiv \hat{i}\frac{\partial}{\partial x} + \hat{j}\frac{\partial}{\partial y} + \hat{k}\frac{\partial}{\partial z}$ the del operator and $\overleftrightarrow{D}$ the diffusion tensor. Here $\hat{i}$, $\hat{j}$ and $\hat{k}$ represent the unit vector in the x-, y- and z-axis, respectively.

Following Stejskal [6] the magnetic field can be written as

$$\vec{H} = [H_0 + (\vec{r} \cdot \vec{G})]\hat{k} \tag{2}$$

where H_0 is the static magnetic field, $\vec{r}$ the spatial location vector and $\vec{G}(t)$ the applied magnetic field gradient which is assumed to be uniform throughout the sample. Substituting Eq. (2) into Eq. (1) and combining the two equations for M_x and M_y into one equation we obtain

$$\partial m/\partial t = -i\omega_0 m - m/T_2 - i\gamma \vec{r} \cdot \vec{G} m + \vec{\nabla} \cdot \overleftrightarrow{D} \cdot \vec{\nabla} m, \tag{3}$$

where $m \equiv M_x + iM_y$, $i = \sqrt{-1}$ and $\omega_0 = \gamma H_0$ the Larmor precession frequency. The last term on the right-hand side of Eq. (3) can be expanded to include two terms, specifically,

$$\vec{\nabla} \cdot \overleftrightarrow{D} \cdot \vec{\nabla} m = (\vec{\nabla} \cdot \overleftrightarrow{D}) \cdot \vec{\nabla} m + \overleftrightarrow{D} : \vec{\nabla}\vec{\nabla} m \tag{4}$$

where $(\vec{\nabla} \cdot \overleftrightarrow{D})$ means that the operator $\vec{\nabla}$ acts on $\overleftrightarrow{D}$ only, i.e., $(\vec{\nabla} \cdot \overleftrightarrow{D}) \cdot \vec{\nabla} m = \sum_{i,j=1}^{3} \frac{\partial D_{ij}}{\partial x_i} \cdot \frac{\partial m}{\partial x_j}$ and ":" represents the generalized dot product of tensor, i.e., $\overleftrightarrow{D} : \vec{\nabla}\vec{\nabla} m = \sum_{i,j=1}^{3} D_{ij} \frac{\partial^2 m}{\partial x_i \partial x_j}$, respectively.

For any selected voxel, the diffusion tensor $\overleftrightarrow{D}$ varies with $\vec{r}$ within the voxel, and we can expand $\overleftrightarrow{D}$ around the center location $\vec{r}_0$ of the voxel,

$$\overleftrightarrow{D}(\vec{r}) = \overleftrightarrow{D}(\vec{r}_0) + (\vec{r} - \vec{r}_0) \cdot [\vec{\nabla} \overleftrightarrow{D}(\vec{r})]|_{\vec{r}=\vec{r}_0} + \cdots \tag{5}$$

where $[\vec{\nabla} \overleftrightarrow{D}(\vec{r})]|_{\vec{r}=\vec{r}_0} = \partial D_{jk}(\vec{r})/\partial x_i|_{\vec{r}=\vec{r}_0}$ and "..." represents the high-order terms. Since $\overleftrightarrow{D}(\vec{r}_0)$ is a constant tensor and therefore $\vec{\nabla} \cdot \overleftrightarrow{D}(\vec{r}_0) = 0$, we have

$$\vec{\nabla} \cdot \overleftrightarrow{D}(\vec{r}) = \vec{K}(\vec{r}_0) + \cdots \tag{6}$$

where $\vec{K}(\vec{r}_0) = \vec{\nabla} \cdot \overleftrightarrow{D}(\vec{r})|_{\vec{r}=\vec{r}_0} = \sum_{i=1}^{3} \frac{\partial D_{ij}(\vec{r})}{\partial x_i}|_{\vec{r}=\vec{r}_0}$.

Comparing with the leading terms $\overleftrightarrow{D}(\vec{r}_0)$ in Eq. (5) and $\vec{K}(\vec{r}_0)$ in Eq. (6), we assume that the effect caused by all other high-order terms can be neglected. Eq. (3) reduces to

$$\partial m/\partial t = -i\omega_0 m - m/T_2 - i\gamma \vec{r}\cdot\vec{G}m + \vec{K}\cdot\vec{\nabla}m + \overleftrightarrow{D}:\vec{\nabla}\vec{\nabla}m, \tag{7}$$

where $\vec{K} = \vec{K}(\vec{r}_0)$ is a constant vector and $\overleftrightarrow{D} = \overleftrightarrow{D}(\vec{r}_0)$ a constant tensor.

We solve Eq. (7) for a spin echo pulse sequence (Fig. 1) as shown below.

For $0<t<\tau=\mathrm{TE}/2$, we first define $\psi(t)$ by means of expression

$$m(\vec{r},t) = \psi(t)\exp\left[-i\omega_0 t - t/T_2 - i\gamma\vec{r}\cdot\vec{F}(t)\right], \tag{8}$$

where $\vec{F}(t) = \int_0^t \vec{G}(t')\mathrm{d}t'$. Substituting Eq. (8) into Eq. (7) yields

$$\mathrm{d}\ln\psi/\mathrm{d}t = -i\gamma\vec{K}\cdot\vec{F}(t) - \gamma^2\vec{F}(t)\cdot\overleftrightarrow{D}\cdot\vec{F}(t). \tag{9}$$

Integrating Eq. (9) yields the solution for $\psi(t)$, and substituting the solution into Eq. (8) we have

$$\begin{aligned} m(\vec{r},t) = m_0\ \exp\ [&-i\omega_0 t - t/T_2 \\ &- i\gamma\vec{r}\cdot\vec{F} - i\gamma\vec{K}\cdot\int_0^t \vec{F}\,\mathrm{d}t' \\ &- \gamma^2\int_0^t \vec{F}\cdot\overleftrightarrow{D}\cdot\vec{F}\,\mathrm{d}t'], \end{aligned} \tag{10}$$

where m_0 is the initial value of $m(\vec{r},t)$ right after the 90° pulse.

For $t>\tau$, we then define $\psi(t)$ by

$$m(\vec{r},t) = \psi(t)\ \exp\ [-i\omega_0(t-2\tau) - t/T_2 - i\gamma\vec{r}\cdot\vec{E}(t)], \tag{11}$$

where $\vec{E}(t) = \int_\tau^t \vec{G}(t')\mathrm{d}t' - \vec{F}(\tau)$. Substituting Eq. (11) into Eq. (7) yields

$$\mathrm{d}\ln\psi/\mathrm{d}t = -i\gamma\vec{K}\cdot\vec{E}(t) - \gamma^2\vec{E}(t)\cdot\overleftrightarrow{D}\cdot\vec{E}(t) \tag{12}$$

Integrating Eq. (12) yields the solution for $\psi(t)$. We write the final solution for $m(\vec{r},t)$:

$$m\left(\vec{r},t\right) = m_0 \mathrm{e}^{-i\omega_0(t-2\tau) - \frac{t}{T_2} - i\gamma\vec{r}\cdot\vec{E} + i\gamma\vec{K}\cdot\int_0^\tau \vec{\mathrm{F}}\,\mathrm{d}t - i\gamma\vec{K}\cdot\int_\tau^t \vec{E}\,\mathrm{d}t' - \gamma^2\int_0^\tau \vec{F}\cdot\overleftrightarrow{D}\cdot\vec{F}\,\mathrm{d}t - \gamma^2\int_\tau^t \vec{E}\cdot\overleftrightarrow{D}\cdot\vec{E}\,\mathrm{d}t'} \tag{13}$$

In obtaining Eq. (13), we used the boundary condition $m(\vec{r},\tau^-) = m^*(\vec{r},\tau^-)$, where $m(\vec{r},\tau^-)$ is the value of $m(\vec{r},t)$ right before the 180° pulse and $m(\vec{r},\tau^+)$ the value of $m(\vec{r},t)$ right after the 180° pulse.

At the echo time, we have

$$m\left(\vec{r},\mathrm{TE}\right) = m_0 \mathrm{e}^{\frac{\mathrm{TE}}{T_2} - i\gamma\vec{r}\cdot\vec{E}(2\tau) + i\gamma\vec{\mathrm{K}}\cdot\int_0^\tau \vec{F}\,\mathrm{d}t - i\gamma\vec{K}\cdot\int_\tau^{2\tau}\vec{E}\,\mathrm{d}t' - \gamma^2\int_0^\tau \vec{\mathrm{F}}\cdot\overleftrightarrow{D}\cdot\vec{F}\,\mathrm{d}t - \gamma^2\int_\tau^{2\tau}\vec{E}\cdot\overleftrightarrow{D}\cdot\vec{E}\,\mathrm{d}t'}. \tag{14}$$

For the symmetric trapezoidal pulses in Fig. 1, calculating and combining all integration terms in Eq. (14) yield

$$m(\vec{G}) = m(0)\mathrm{e}^{i\vec{d}\cdot\vec{K} - \overleftrightarrow{b}:\overleftrightarrow{D}} \tag{15}$$

where $m(\vec{G})$ is the echo MR signal in the presence of the diffusion-encoding magnetic field gradient $\vec{G}$ (DEG), $m(0)$ the echo MR signal without diffusion-weighting ($\vec{G} = 0$), $\vec{d} \equiv \gamma\delta\Delta\vec{G}$, or $d_i \equiv \gamma\delta\Delta G_i$ and

$\overleftrightarrow{b} \equiv \gamma^2\left[\delta^2\left(\Delta - \frac{\delta}{3}\right) + \frac{\varepsilon^3}{30} - \frac{\delta\varepsilon^2}{6}\right]\vec{G}\,\vec{G}$, or

$b_{ij} \equiv \gamma^2\left[\delta^2\left(\Delta - \frac{\delta}{3}\right) + \frac{\varepsilon^3}{30} - \frac{\delta\varepsilon^2}{6}\right]G_iG_j$. Just as $\overleftrightarrow{b}$ characterizes the diffusion effect, the new parameter $\vec{d}$ characterizes the diffusion gradient effect. In the absence of diffusion gradient, i.e., $K = 0$, Eq. (15) is identical to the Eq. (10) in Basser et al. [7] which was used to estimate $\overleftrightarrow{D}$ in DTI. As can be seen, $\overleftrightarrow{D}$ attenuates the echo intensity of the MR signal, but K causes a phase shift in the echo signal. Letting A and ϕ be the echo intensity and phase of the MR signal, i.e., $m = A\mathrm{e}^{i\phi}$, we found that

$$\ln\left[\frac{A(\vec{G})}{A(0)}\right] = -\sum_{i,j=1}^{3} b_{ij}D_{ji} \tag{16a}$$

$$\phi(\vec{G}) - \phi(0) = \sum_{i=1}^{3} d_iK_i \tag{16b}$$

where

$$\begin{aligned} &A(\vec{G}) = \sqrt{\mathrm{Re}(m(\vec{G}))^2 + \mathrm{Im}(m(\vec{G}))^2} \text{ and} \\ &A(0) = \sqrt{\mathrm{Re}(m(0))^2 + \mathrm{Im}(m(0))^2}, \end{aligned} \tag{17a}$$

$$\begin{aligned} \phi\left(\vec{G}\right) &= \tan^{-1}\left(\frac{\mathrm{Im}(m(\vec{G}))}{\mathrm{Re}(m(\vec{G}))}\right) \text{ and } \phi(0) \\ &= \tan^{-1}\left(\frac{\mathrm{Im}(m(0))}{\mathrm{Re}(m(0))}\right) \end{aligned} \tag{17b}$$

Here, Re and Im represent the real and imaginary part of the echo signal, respectively. Eqs. (16a) and (16b) show that $\overleftrightarrow{D}$ is determined from the echo intensity and $\vec{K}$ from the echo phase, respectively. Since an MRI scan is capable of providing both intensity and phase images, Eqs. (16a) and (16b) show that both $\overleftrightarrow{D}$ and $\vec{K}$ can be determined simultaneously, i.e., no additional data acquisition is needed for determining $\vec{K}$. According to Eq. (16b), the phase shift, with and without a DEG, determines the component of $\vec{K}$ in the direction of the DEG, resulting in diffusion gradient-weighted MRI (DGWI).

The six independent components of $\vec{D}$ in Eq. (16a) and three components of $\vec{K}$ in Eq. (16b) can be simultaneously determined from the echo intensities and phase shifts of diffusion-weighted images encoded in six noncollinear directions of the applied DEGs, along with an image acquired without diffusion weighting (b=0) for $A(0)$ and $\phi(0)$. Let $X=[x_1\ x_2\ x_3\ x_4\ x_5\ x_6]^{\mathrm{T}}$ and $Y=[y_1\ y_2\ y_3\ y_4\ y_5\ y_6]^{\mathrm{T}}$ be a 6×1 matrix that stores these six observations of the left side of Eq. (16a) and of Eq. (16b), respectively. We define a 6×1 matrix as $\alpha=[D_{xx}\ D_{yy}\ D_{zz}\ D_{xy}\ D_{xz}\ D_{yz}]^{\mathrm{T}}$, which represents the six tensor components in Eq. (16a), and a 3×1 matrix as $\beta=[K_1\ K_2\ K_3]^{\mathrm{T}}$, which represents the three components of $\vec{K}$ in Eq. (16b), respectively. Let ξ and φ be the predicted outcomes according to Eqs. (16a) and (16b), i.e.,

$$\xi = B\alpha \tag{18a}$$

$$\varphi = \Sigma\beta \tag{18b}$$

where B is a 6×6 matrix that is computed from the right side of Eq. (16a) and Σ a 6×3 matrix that is computed from the right side of Eq. (16b), respectively. The method of least-squares regression can be used to yield the optimal estimations for both α and β. To do so, we construct two parameters χ_1^2 and χ_2^2, defined as

$$\chi_1^2 = (X-\xi)^{\mathrm{T}}(X-\xi) \tag{19a}$$

$$\chi_2^2 = (Y-\varphi)^{\mathrm{T}}(X-\varphi) \tag{19b}$$

where χ_1^2 is the sum of squares of deviations between the observed and the predicted echo intensities, and, χ_2^2, the sum of squares of deviations between the observed and the predicted echo phases, respectively. Minimizing χ_1^2 with respect to each of the six unknown parameters in α yields the equation for the optimal parameters,

$$\alpha_{\mathrm{opt}} = (B^{\mathrm{T}}B)^{-1}B^{\mathrm{T}}X. \tag{20a}$$

Similarly, minimizing χ_2^2 with respect to each of the three unknown parameters in β yields the optimal parameters,

$$\beta_{\mathrm{opt}} = (\Sigma^{\mathrm{T}}\Sigma)^{-1}\Sigma^{\mathrm{T}}Y. \tag{20b}$$

The diagonalization of the diffusion tensor provides a simpler way to extract the diffusion anisotropy effects from the measured six independent components of the tensor [7].

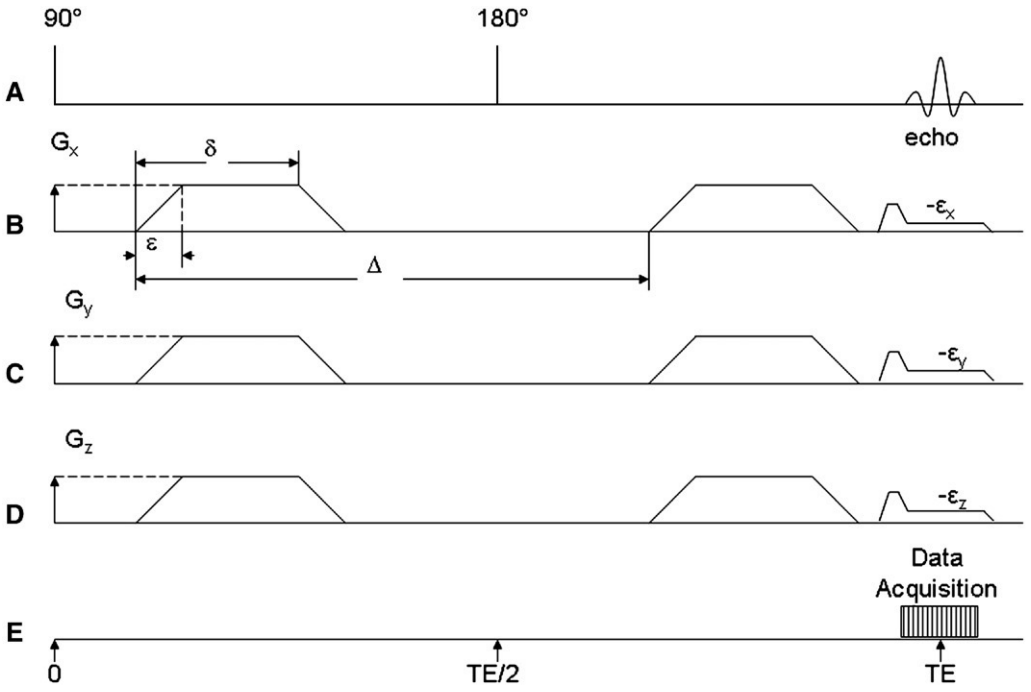

Fig. 1. Illustrative waveforms for a spin echo diffusion pulse sequence: (A) the 90° and 180° RF pulses, and the echo signal; magnetic field gradients applied in the (B) x-axis, (C) y-axis and (D) z-axis; (E) the time line and data acquisition window. TE is the echo time, δ the time between the initial rise of the trapezoidal pulse and the end of its plateau, Δ the time between the initial rise of the first and second pulses, and ε the rise time of the ramp. G_x, G_y and G_z are the maximum field gradients along the axes of x, y and z, respectively. The three gradient pulses applied during the acquisition window compensate the corresponding DEG-induced linear EC terms, and the three initial pulses applied just before the acquisition compensate the cumulated phase shifts prior to the acquisition due to the linear EC terms.

To diagonalize the tensor $\overleftrightarrow{D}$, it is necessary to solve the characteristic equation of $\overleftrightarrow{D}$:

$$|\overleftrightarrow{D}-\lambda\overleftrightarrow{I}|=0, \tag{21}$$

where $\overleftrightarrow{I}$ represents the isotropic identity tensor or the 3×3 unit matrix. The solution of Eq. (21) yields three eigenvalues λ_i and three corresponding eigenvectors $\vec{\varepsilon}_i$, satisfying the same set of matrix equations:

$$(\overleftrightarrow{D}-\lambda_i\overleftrightarrow{I})\,\vec{\varepsilon}_i=0,\ (i=1,2,3). \tag{22}$$

The three eigenvectors are orthogonal to each other, forming an orthogonal coordinate system. In this principal coordinate system (u,v,w), the diffusion tensor becomes diagonal,

$$\overleftrightarrow{D}=\begin{pmatrix}\lambda_u & 0 & 0\\ 0 & \lambda_v & 0\\ 0 & 0 & \lambda_w\end{pmatrix}. \tag{23}$$

These three orthonormal eigenvectors also form a rotation transformation from the laboratory coordinate system to the principal coordinate system. Applying this transformation to $\vec{K}=\nabla\cdot\overleftrightarrow{D}$ yields

$$\frac{\partial\lambda_i}{\partial u_i}=\sum_{j=1}^{3}\varepsilon_{ij}K_j \tag{24}$$

where the left side represents the spatial derivatives of the three principal diffusivities in the principal coordinate frame, which elucidates the physical meaning of the diffusion gradient $\vec{K}$.

2.2. Characterization and correction of EC artifacts

According to Eq. (16b), we need to measure the difference of the phase images with and without DEGs in order to determine the diffusion gradient $\vec{K}$. However, the turning on and off of these large DEGs produce ECs which cause a variety of phase artifacts in the phase images [13], in addition to the familiar image distortions [14]. Thus, for a precise measurement of the diffusion gradient these large phase errors caused by the DEG-induced EC must be corrected.

Within the data acquisition window the DEG induces a time-varying EC as

$$\vec{B}_{\mathrm{EC}}(t)=[\varepsilon_0(t)+\varepsilon_x(t)x+\varepsilon_y(t)y+\varepsilon_z(t)z]\hat{B}_0 \tag{25}$$

where $\hat{B}_0$ represents the unit vector of the main field [14]. When a spatially symmetric uniform phantom is placed at the center of the magnet with all phase- and frequency-encoding gradients turned off, assuming that the slice-selection is the y-axis, the signal acquired at time t with the DEG in an arbitrary direction is given by

$$S_{\mathrm{on}}(y_0,t)=S_0\ \exp\ [i\phi_{\mathrm{on}}(y_0,t)] \tag{26a}$$

$$\varphi_{\mathrm{on}}(y_0,t)=-\gamma\int_0^t[\varepsilon_0(t')+\varepsilon_y(t')\cdot y_0]\mathrm{d}t'+\Phi_{\mathrm{off}}(y_0,t) \tag{26b}$$

where $\Phi_{\mathrm{off}}(y_0,t)$ represents the cumulated phase with the DEG turned off. Thus the difference in phase with and without the DEG turned on is

$$\Delta\phi_{\mathrm{on}}(y_0,t)=\phi_0(t)+y_0\varphi_y(t) \tag{27}$$

where $\phi_0(t)=-\gamma\int_0^t\varepsilon_0(t')\mathrm{d}t'$ and $\varphi_y(t)=-\gamma\int_0^t\varepsilon_y(t')\mathrm{d}t'$. Based on the measurements at two slice positions y_1 and y_2, the following can be obtained:

$$\phi_0(t)=[y_2\Delta\phi_{\mathrm{on}}(y_1,t)-y_1\Delta\phi_{\mathrm{on}}(y_2,t)]/(y_2-y_1) \tag{28a}$$

$$\varphi_y(t)=[\Delta\phi_{\mathrm{on}}(y_1,t)-\Delta\phi_{\mathrm{on}}(y_2,t)]/(y_1-y_2) \tag{28b}$$

Optimal estimations for $\phi_0(t)$ and $\varphi_y(t)$ can be obtained by a polynomial or exponential curve fitting of the measured $\phi_0(t)$ and $\varphi_y(t)$, respectively. With these estimations, both $\varepsilon_0(t)$ and $\varepsilon_y(t)$ can be computed for each time point in the data acquisition window and, similarly, $\varepsilon_x(t)$ and $\varepsilon_z(t)$. It was found that both the zero-order and first-order EC terms were approximately constant within the data acquisition window [13].

The zero term $\varepsilon_0(t)$ causes a fixed phase shift, $\Delta\phi=-\gamma\int_0^{\mathrm{TE}-\mathrm{Ts}/2}\varepsilon_0(t)\mathrm{d}t$, in the diffusion-weighted phase image relative to the phase image without the DEG. Within the sampling window Ts, $\varepsilon_0(t)$ remains approximately a constant [13] that causes an overall position shift in the frequency-encoding direction. These two overall phase and position shifts due to the zero EC term can be corrected during post-processing with the measured $\Delta\phi$ and $\varepsilon_0(t)$. To examine the effects due to the linear (first-order) EC terms, we assume that x is the frequency-encoding axis, y the phase-encoding axis and z the slice-selection axis. Within each slice, the linear term $\varepsilon_z(t)$ causes an additional overall phase shift, $\delta\varphi=-\gamma z\int_0^{\mathrm{TE}-\mathrm{Ts}/2}\varepsilon_z(t)\mathrm{d}t$. The other two linear terms $\varepsilon_x(t)$ and $\varepsilon_y(t)$ cause a k-space center shift with $\delta k_x=-\frac{\gamma}{2\pi}\int_0^{\mathrm{TE}-\mathrm{Ts}/2}\varepsilon_x(t)\mathrm{d}t$ and $\delta k_y=-\frac{\gamma}{2\pi}\int_0^{\mathrm{TE}-\mathrm{Ts}/2}\varepsilon_y(t)\mathrm{d}t$, respectively. δk_x yields a linear phase variation along the x-axis with a slope of $2\pi\delta k_x\Delta x$ (radians per pixel), where Δx is the pixel size. Similarly, δk_y also yields a linear phase variation along the y-axis with a slope of $2\pi\delta k_y\Delta y$ (radians per pixel). The overall phase shift $\delta\phi$ and the two linear phase variations along the x- and y-axes can be derived and used to correct the diffusion-weighted phase images, resulting in artifact-free phase images. They can also be corrected with three EC-compensation gradient pulses in x-, y- and z-axes applied just before the acquisition window (see Fig. 1). Within the sampling window, all three linear terms $\varepsilon_x(t)$, $\varepsilon_y(t)$ and $\varepsilon_z(t)$ remain approximately constants [13]. Like $\varepsilon_0(t)$, $\varepsilon_z(t)$ also causes an overall position shift in the x-axis, which can also be corrected during post-processing with the measured $\varepsilon_z(t)$. However, the read direction linear term $\varepsilon_x(t)$ causes a size change to the object image and the phase direction linear term $\varepsilon_y(t)$ causes an image shearing. With the measured linear EC terms, these three geometric distortions can be corrected by applying three EC-compensation gradient pulses $\vec{B}_{\mathrm{COMP}}(t)=-[\varepsilon_x(t)x+\varepsilon_y(t)y+\varepsilon_z(t)z]\hat{B}_0$

during the acquisition window, resulting in geometric distortion-free diffusion-weighted images (see Fig. 1).

2.3. Potential application of DGWI in delineating tissue interfaces

Like the parameter $\overleftrightarrow{b}$ in Eq. (15) which characterizes the diffusion effect on the magnitude image, the parameter $\vec{d}$ in Eq. (15) characterizes the diffusion gradient effect on the phase image. The larger the $\vec{d}$, the greater the diffusion gradient effect. However, increasing $\vec{d}$ inevitably requires increasing $\overleftrightarrow{b}$, which in turn decreases the signal-to-noise ratio (SNR) of diffusion-weighted magnitude images. A decrease in SNR increases error in phase measurements [15]. Thus, optimization of the diffusion gradient effect ought to make $\vec{d}$ as large as possible while keeping $\overleftrightarrow{b}$ almost unchanged. Since $b\approx\gamma^2G^2\delta^2(\Delta-\delta/3)$ and $d=\gamma G\delta\Delta$, for a given TE, choosing a right combination of Δ, δ and G may optimize the diffusion gradient effect. For example, for a given TE=75 ms and $b\approx1000$ (s/mm^2), we have d=7.54 (s rad/mm) for Δ=52 ms, δ=14 ms and G=4.0 (g/cm), but d=6.14 (s rad/mm) for Δ=29 ms, δ=20 ms and G=4.0 (g/cm).

One potential application of DGWI is to delineate the interface of two tissues with markedly different diffusion properties. When water diffusion is dramatically different in one tissue than another, this difference yields a large diffusion gradient across the interface. The magnitude of diffusion gradient effect on phase change depends on the d value and the voxel-averaged magnitude of $\vec{K}$ along the direction of diffusion-encoding gradient pulses [Eq. (16b)]. We use the interface between the cerebrospinal fluid (CSF) and GM as an example to estimate the phase change caused by the diffusion gradient across the interface. We assume that the direction of diffusion-encoding gradient pulses is perpendicular to the interface, and consider a pixel on the interface that evenly covers the two sides. For a typical FOV 240 mm with a matrix size 128×128, the in-plane spatial resolution of the pixel is 1.875 mm. Thus, the distance between the center of the half-pixel on the CSF side and the center of the other half-pixel on the GM side is 0.94 mm. With the measured mean diffusivity of 3.19×10^{-3} (mm^2/s) for CSF and 0.83×10^{-3} (mm^2/s) for GM [8], we estimate a magnitude of 2.51×10^{-3} (mm/s) for $\vec{K}$ in the direction perpendicular to the interface. With d=7.54 (s·radian/mm), we have an estimated phase change of 0.019 rad at the interface due to the diffusion gradient effect. If this diffusion gradient-induced phase change on the interface can be measured, then it offers an objective measure for delineating the interface.

3. Methods and materials

3.1. EC measurement

A spin echo pulse sequence was developed to include DEG, an option to turn off the phase- and frequency-encoding gradients for measuring the EC terms, and three EC-compensation gradient pulses to compensate for the EC phase artifacts produced by the linear EC terms. To verify the effectiveness of correction for EC phase artifacts, a dimethyl silicone spherical phantom with a diameter of ~15 cm was used. Since the diffusion coefficient of the silicone oil is almost zero, the diffusion effect on the silicon phantom is very small and its effect on the EC measurement should be negligible. Two axial slices were acquired on a GE 3.0-T clinical scanner (General Electric HealthCare, Milwaukee, WI, USA) with a quadrature *head* coil, FOV=240 mm, matrix size 128×128, TE/TR=75/1000 ms, slice thickness 3 mm, NEX 1, b=1000 (s/mm^2) and d=6.02 (s·radian/mm). The DEG was applied along the x-axis. Inhouse-developed software was used for image reconstruction and computation.

3.2. Correction of the k-space off-center shift

In the absence of DEG, when the phase- and frequency-encoding gradients were turned on, the Fourier transform of the raw data yielded a phase image for each slice (the left image in Fig. 2). This image is not uniform; the top side is brighter than the bottom side and the right side is slightly brighter than the left side, respectively. The phase variations in both frequency and phase directions were due to a small offset of the k-space center that arose with the discrete Fourier transform and the offset is less than 1 pixel. These phase variations were corrected first prior to any EC correction. A large square white box was selected as a region of interest (ROI). Within the ROI, the slope of the phase as a function of position was computed first for each line in the frequency-encoding direction, and then the mean of these slopes was calculated for that direction. The mean slope of the phase for the phase-encoding direction was obtained in the same way. These slopes were then used to determine the k-space off-center shifts in both the frequency and phase directions. The shifts were then used to correct these phase variations during image reconstruction, resulting in a uniform phase image for the uniform phantom [the right image in Fig. 2 and the left image in Fig. 3(A)].

3.3. EC Calculation and correction

The raw data with the phase- and frequency-encoding gradients off were used to compute the overall phase shift $\Delta\phi$ caused by the zero EC term $\varepsilon_0(t)$, the overall phase shift $\delta\phi$ caused by the linear EC term $\varepsilon_z(t)$ and the two k-space center shifts δk_x and δk_y that were caused by the two linear EC terms $\varepsilon_x(t)$ and $\varepsilon_y(t)$, respectively. These calculations were straightforward as outlined previously. These measured values could be used to correct the EC effects on the phase image during image reconstruction. Alternatively, because the effects on the phase image due to these EC terms are known, the total overall phase shift ($\Delta\phi+\delta\phi$) could also be determined from the phase difference between the phase image with DEG and the phase image without DEG. Similarly, the two k-space center shifts δk_x and δk_y could also be determined from the two slopes of the phase along the

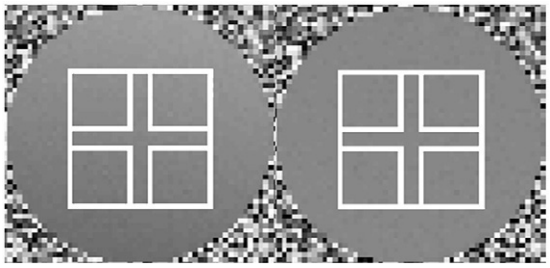

Fig. 2. Phase images without DEG. Left: The phase image without correcting the *k*-space off-center shift aroused from the discrete Fourier transform. Right: The phase image with the correction.

frequency and phase directions, respectively. These determined values could also be used to correct these EC effects during the image reconstruction. Fig. 3(C,D) was obtained with this method. The determined values for δk_x and δk_y were also used for the EC-compensation gradient pulses $\vec{B}_{\mathrm{COMP}}(t)$ during data acquisition (Fig. 1), and the corresponding EC-compensated phase image is shown in Fig. 3(E).

3.4. Phase contrast induced by DEG

To image the effect of diffusion gradients on the phase images with DEG, a small sample consisting of a piece of chicken thigh placed in a saline solution was scanned with a clinical quadrature *wrist* coil, aiming to qualitatively demonstrate the diffusion gradient-induced phase change at the interface between the tissue and the solution. The FOV was 60 mm, and all the other parameters were the same as above. This fourfold decrease in FOV produced a fourfold increase in the in-plane spatial resolution, resulting in a fourfold increase in the magnitude of the diffusion gradient-induced phase change at the interface. A DEG was applied on both the *x*- and *y*-axes with the same *b* and *d* values as above.

4. Results

The left image in Fig. 2 shows the phase image of one slice without DEG, and the right one shows the phase image with the correction of the small offset of the *k*-space center that arose with the discrete Fourier transform. To verify the effectiveness of this correction, four same size but smaller white boxes were selected inside the large ROI. The phase variations in the left image were well demonstrated with the different means and standard deviations for the five ROIs: 2.86±0.21 rad for the large box, 3.01±0.10 rad for the top left small box, 3.10±0.10 rad for the top right small box, 2.62±0.10 rad for the bottom left small box and 2.72±0.10 rad for the bottom right small box. Correspondingly, for the right image the mean and standard deviation for the five ROIs were 2.89±0.04, 2.89 ±0.04, 2.90±0.04, 2.89±0.04 and 2.89±0.04 rad, respectively. The observed same mean and standard deviation for the five ROIs show the effectiveness of the correction. This phase-corrected image served as the reference for DEG-induced phase variations, and, accordingly, the same *k*-space off-center correction was applied to the phase images with the DEG.

Relative to the reference phase image in Fig. 3(A), the effect of DEG-induced EC terms on the phase image is shown in Fig. 3(B). The applied DEG produced an overall phase shift to the mean value of 2.412±0.181 rad at the ROI (white box) from the mean value of 2.895±0.041 rad without DEG. As discussed previously, this overall phase shift was from the cumulated phase shift of $\Delta\phi$ and $\delta\phi$ due to the zero EC term $\varepsilon_0(t)$ and the linear EC term $\varepsilon_z(t)$. After the correction of this overall phase shift, the two linear phase variations in the frequency and phase directions due to the other two linear EC terms $\varepsilon_x(t)$ and $\varepsilon_y(t)$ are shown in Fig. 3 (C). These linear phase variations were well reflected in the dramatically increased standard deviation (0.181 rad) of the ROI relative to 0.041 rad, the standard deviation for the reference without DEG. The two mean slopes for these two linear phase variations were computed and then the two corresponding *k*-space center shifts δk_x and δk_y were further calculated. With these δk_x and δk_y determined, a post-processing phase correction was applied during image reconstruction to eliminate these EC-induced linear phase variations, resulting in the EC artifact-free phase image [Fig. 3(D)] with a mean phase value of 2.915±0.043 rad at the ROI. The two values for δk_x and δk_y were also used for

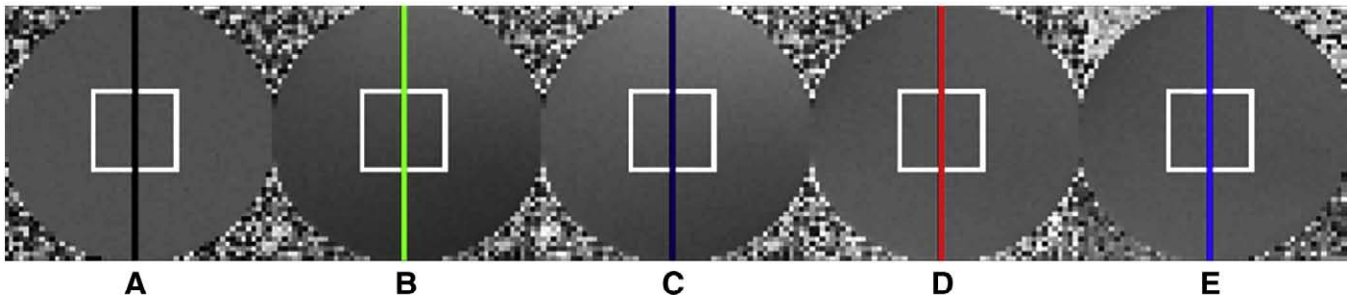

Fig. 3. Phase images with DEG. (A) The reference phase image without DEG; (B) the phase image with DEG; (C) the phase image with the correction of the overall phase shift due to the cumulated overall phase shift induced by the zero EC term $\varepsilon_0(t)$ and the linear EC term $\varepsilon_z(t)$; (D) the phase image with the correction of the linear phase variations due to the linear EC terms $\varepsilon_x(t)$ and $\varepsilon_y(t)$; and (E) the phase image with the EC-compensation gradient pulses.

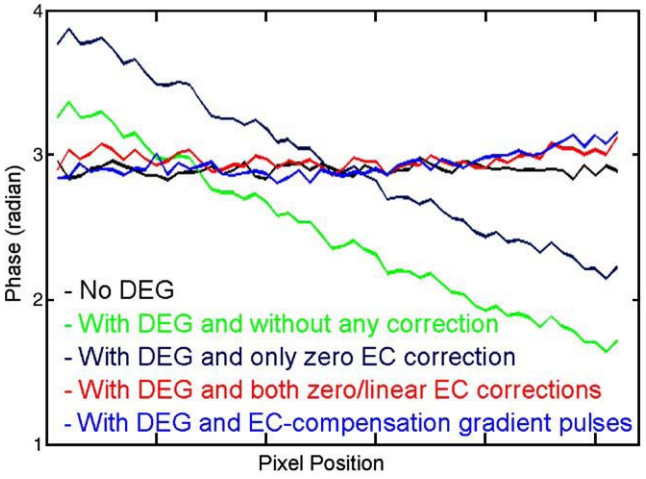

Fig. 4. Plots of phase values of the five colored lines in Fig. 3.

compensating these EC-induced linear phase variations with the EC-compensation gradient pulses, as illustrated in Fig. 1, resulting in the EC-compensated phase image [Fig. 3(E)] with a mean phase value of 2.879±0.043 rad at the ROI. These results demonstrate that the DEG-induced EC phase artifacts can be effectively corrected either during post-processing or using EC-compensation gradient pulses, as shown in Fig. 4.

Fig. 5 shows the magnitude and phase images of the tissue sample with and without DEG. In the absence of DEG, the magnitude image of the sample (top left in Fig. 5) clearly differentiated the tissue (the relative dark part in the bottom) from the solution (the relative bright part in the top), but no differences were presented in the phase image (bottom left in Fig. 5). In the presence of the DEG, however, the DEG not only attenuated the magnitude image as expected (top right in Fig. 5), but also induced an apparent difference in the phase image, particularly at the interface (bottom right in Fig. 5). (Note that no phase corrections were made on these two phase images.) This noticeable phase contrast induced by the DEG at the interface is consistent with our theory.

5. Discussion and conclusions

Unlike water diffusion which attenuates the magnitude of MR signals, the spatial derivative of water diffusion produces a phase change to the MR signal as shown in Eq. (15). Since the phase of an MR signal can be measured, Eq. (15) offers a novel technique for measuring the diffusion gradient. However, the magnetic field gradient pulses that encode the effect of water diffusion have such high magnitudes that they can induce large ECs which in turn produce large phase artifacts, rendering the phase measurement in error if these EC-induced phase artifacts are not corrected. As demonstrated in Figs. 3(D,E) and 4, these DEG-induced EC phase artifacts can be effectively corrected either during post-processing or with EC-compensation gradient pulses, resulting in almost artifact-free images and making it possible to measure diffusion gradients reliably.

Although this study demonstrates the potential of the presented technique for measuring diffusion gradients, its feasibility mainly depends on the magnitude of diffusion gradient-induced phase change relative to the unavoidable noise-induced phase changes. As shown in Eq. (15), the diffusion gradient-induced phase change depends on the product of the d value and the voxel-averaged magnitude of $\vec{K}$ along the direction of diffusion-encoding gradient pulses. Like the parameter b which characterizes the diffusion effect on the magnitude image, the parameter d characterizes the diffusion gradient effect on the phase image, and this diffusion gradient effect increases with the d value. However, increasing d inevitably causes the increase of the b value, which in turn leads to the reduction of the SNR for the diffusion-weighted magnitude images. A decreased SNR will increase the standard deviation of phase accordingly [15], resulting in an increase of the noise-induced phase changes in the phase measurement. Thus, optimization of the diffusion gradient effect ought to make d as large as possible while making b as small as possible.

The magnitude of diffusion gradient-induced phase change is not expected to be large except at the interfaces of tissues with markedly different diffusion properties, making it a challenge to measure diffusion gradients reliably. When the magnitude of diffusion gradient-induced phase change is not significantly larger than the noise-induced phase change, it would be very difficult, if not impossible, to separate the diffusion gradient-induced phase change from the noise-induced phase change. The unavoidable noise-induced phase changes are measured by the standard deviation of phase in phase images. This standard deviation

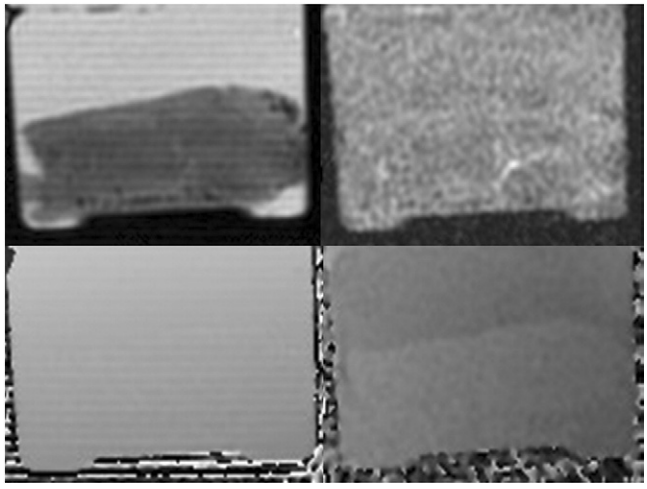

Fig. 5. DGWI of a tissue sample. The left column represents the magnitude image (top) and the phase image (bottom) in the absence of DEG, and the right column presents the magnitude image (top) and the phase image (bottom) with the DEG. The bright part in the magnitude image without DEG was the image of the solution, and the relative dark part was the image of the tissue. Note that no phase corrections were applied to these two phase images.

of phase imposes a statistically lower limit for measuring diffusion gradient-induced phase changes. One effective way to reduce the noise-induced phase changes is to increase the number of excitations, but with the penalty of an increased total scan time.

One potential application of DGWI, as demonstrated by our preliminary result with a tissue sample, is to delineate the interface of two tissues with markedly different diffusion properties (Fig. 5). Although a more quantitative study is required to verify this novel technique, this preliminary observation appears to support our theory. A more quantitative study should include the measurement of both the zero and linear EC terms, and then using the obtained EC terms to correct EC artifacts either during the post-processing analysis or using EC-compensation gradients as shown in Fig. 1. As demonstrated in Figs. 3 and 4, it would be impossible to obtain reliable phase measurement without the EC correction. The quantitative study should also include the measurement of the diffusion gradient at the interface of the tissue sample and the measurement of the diffusion coefficients of the solution and the tissue. The measured diffusion coefficients would then be used to compute the diffusion gradient at the interface. The comparison of the measured diffusion gradient with the computed diffusion gradient would verify the presented theory. (The applied DEG produced an overall phase change of 0.48 radians [Fig. 3(B)], but the diffusion gradient across the interface of the tissue sample was estimated to produce only a small phase change of 0.08 rad at the interface. Thus, the EC-induced phase change dominated and would render the measurement of the diffusion gradient at the interface in error if not corrected. Unfortunately, due to the lack of a small phantom suitable for the wrist coil used in our preliminary experiment, we were unable to perform the EC correction and therefore to conduct such a quantitative study. Accordingly, it rendered our preliminary experiment qualitatively but not quantitatively.) If it proves to be feasible, DGWI provides a high spatial resolution for delineating tissue interfaces to within an image voxel. Note that the higher the spatial resolution of the image, the larger the diffusion gradient-induced effect across the interface. Such an imaging tool may have a potential application in a possible delineation of Brodmann areas because of their different cytoarchitecture and the likelihood of different diffusion properties. However, diffusion gradient-induced phase changes are not expected to be large and measuring these small phase changes remains a challenge to current techniques, particularly for in vivo MRI. More work needs to be done to test the feasibility of the DGWI technique.

We attempted to apply our technique to the human brain, but there were large motion artifacts and the results were not meaningful in terms of demonstrating the basic concepts of our technique. These artifacts are mainly related to motion including possible breathing, cardiac cycle-related pulsations, flow of CSF and involuntary movements. Large phase changes were observed when the DEG was applied. These large motion artifacts are unavoidable with the spin echo diffusion-weighted pulse sequence used in this study, rendering the technique unfeasible for the in vivo scenario. However, these motion artifacts can be effectively eliminated with a spin echo diffusion-weighted echo-planar imaging (EPI) pulse sequence which is much less sensitive to motion. Although the incorporation of the EC correction into the EPI acquisition is straightforward, its implementation is beyond the scope of this study and remains to be investigated.

The theory presented in this study is based on the assumption of the absence of fluid flow. For the in vivo scenario, this assumption is most likely not valid. Tissue microcirculatory flow or "perfusion" in the vascular beds will affect MR signal just like water diffusion would attenuate the signal when diffusion- or flow-encoding gradient pulses are present. A reliable measurement of the effect of perfusion on the MR signal would provide a means of imaging tissue perfusion. Two models for imaging the tissue perfusion have been proposed and investigated: intravoxel incoherent motion (IVIM) and intravoxel coherent motion (IVCM) [1,16–21]. In these studies, different pulse sequences were developed to separate the microcirculatory flow effect from the water diffusion effect. However, one common feature in these studies is the use of gradient pulses to encode these effects, one way or another. As shown previously, these gradient pulses would produce an EC in the data acquisition window, which in turn would yield both geometry distortions to the magnitude image and phase changes to the phase image. The phase changes would directly affect the measurement of IVCM, and the geometry distortions would also affect the measurement of IVIM because these distortions cause signal changes between with and without the gradient pulses. These errors induced by the EC could be eliminated with the EC correction presented in this study, and its effectiveness remains to be explored.

Acknowledgments

We would like to thank Tom Cooper, Jim Lyon and Arnold Wilkins for reading the manuscript and for helpful suggestions. We appreciate Dr. E.J. Potchen and the Department of Radiology at Michigan State University for providing technical support. This work was supported in part by funds from the Department of Radiology at Michigan State University (JH) and in part by the Michigan State University Core Analytical Facility Fund (DCZ).

References

[1] Le Bihan D, Breton E, Lallemand D, Grenier P, Cabanis EA, Laval-Jeantet M. MR imaging of intravoxel incoherent motions: application to diffusion and perfusion in neurologic disorders. Radiology 1986; 161:401–7.

[2] Carr HY, Purcell EM. Effects of diffusion on free precession in nuclear magnetic resonance experiments. Phys Rev 1954;94:630.

[3] Stejskal EO, Tanner JE. Spin diffusion measurements: spin echoes in the presence of a time-dependent field gradient. J Chem Phys 1965;42: 288–92.

[4] Moseley ME, Cohen Y, Mintorovitch J. Early detection of regional cerebral ischemic injury in cats: evaluation of diffusion and T2-weighted MRI and spectroscopy. Magn Reson Med 1990;14:330–46.
[5] Warach S, Chien D, Li W, Ronthal M, Edelman RR. Fast magnetic resonance diffusion-weighted imaging of acute human stroke. Neurology 1992;42:1717–23.
[6] Stejskal EO. Use of spin echoes in a pulsed magnetic-field gradient to study anisotropic, restricted diffusion and flow. J Chem Phys 1965;43: 3597–603.
[7] Basser PJ, Mattiello J, Le Bihan D. Estimation of the effective self-diffusion tensor from the NMR spin echo. J Magn Reson B 1994;103: 247–54.
[8] Pierpaoli C, Jezzard P, Basser P, Barnett A, DiChiro G. Diffusion tensor MR imaging of the human brain. Radiology 1996;201:637–48.
[9] Le Bihan D, Mangin JF, Poupon C, Clark CA, Pappata S, Molko N, et al. Diffusion tensor imaging: concepts and applications. J Magn Reson Imaging 2001;13:534–46.
[10] Moseley ME, Kucharczyk J, Mintorovitch J, et al. Diffusion-weighted MR imaging of acute stroke: correlation with T2-weighted and magnetic susceptibility-enhanced MR imaging in cats. Am J Neuroradiol 1990;11:423–9.
[11] Basser PJ, et al. In vivo fiber tractography using DT-MRI data. Magn Reson Med 2000;44:625–32.
[12] Huang J. Method of measuring diffusion anisotropy and diffusion gradient simultaneously with DTI. Proc Int Soc Magn Reson Med 2006;14:2735.
[13] Huang J, Zhu DC. Correction of Eddy-current induced phase error in diffusion-weighted imaging. Proc Inl Soc Magn Reson Med 2006; 14:2377.
[14] Jezzard P, Barnett AS, Pierpaoli C. Characterization of and correction for Eddy current artifacts in echo planar diffusion imaging. Magn Reson Med 1998;39:801–12.
[15] Haacke EM, Brown RW, Thompson MR, Venkatesan R. Magnetic resonance imaging physical principles and sequence design. New York: Wiley-Liss; 1999. p. 375.
[16] Ahn CB, Lee SY, Nalcioglu O, Cho ZH. The effects of random directional distributed flow in nuclear magnetic resonance imaging. Med Phys 1987;14:43–8.
[17] Le Bihan D, et al. Separation of diffusion and perfusion in intravoxel incoherent motion MR imaging. Radiology 1988;168:497–505.
[18] Young IR, Hall AS, Bryant DJ, Thomas DGT, Gill SS, Dubowitz LMS, et al. Assessment of brain perfusion with MR imaging. J Comput Assist Tomogr 1988;12:721–7.
[19] Turner R, Le Bihan D, Maier J, Vavrek R, Hedges LK, Pekar J. Echo-planar imaging of intravoxel incoherent motion. Radiology 1990;177: 407–14.
[20] Maki JH, MacFall JR, Johnson GA. The use of gradient flow compensation to separate diffusion and microcirculatory flow in MRI. Magn Reson Med 1991;17:95–107.
[21] Jochimsen TH, Norris DG, Mildner T, Moller HE. Quantifying the intra- and extravascular contributions to spin-echo fMRI at 3 T. Magn Reson Med 2004;52:724–32.